

# Proton spectroscopy of $^{48}\text{Ni}$ , $^{46}\text{Fe}$ , and $^{44}\text{Cr}$

M. Pomorski,<sup>1</sup> M. Pfützner,<sup>1,\*</sup> W. Dominik,<sup>1</sup> R. Grzywacz,<sup>2,3</sup> A. Stolz,<sup>4</sup> T. Baumann,<sup>4</sup> J.S. Berryman,<sup>4</sup> H. Czyrkowski,<sup>1</sup> R. Dąbrowski,<sup>1</sup> A. Fijałkowska,<sup>1</sup> T. Ginter,<sup>4</sup> J. Johnson,<sup>3</sup> G. Kamiński,<sup>5,6</sup> N. Larson,<sup>4,7</sup> S.N. Liddick,<sup>4,7</sup> M. Madurga,<sup>2</sup> C. Mazzocchi,<sup>1</sup> S. Mianowski,<sup>1</sup> K. Miernik,<sup>3,1</sup> D. Miller,<sup>2</sup> S. Paulauskas,<sup>2</sup> J. Pereira,<sup>4</sup> K.P. Rykaczewski,<sup>3</sup> and S. Suchyta<sup>4,7</sup>

<sup>1</sup>*Faculty of Physics, University of Warsaw, 00-681 Warsaw, Poland*

<sup>2</sup>*Department of Physics and Astronomy, University of Tennessee, Knoxville, TN 37996, USA*

<sup>3</sup>*Physics Division, Oak Ridge National Laboratory, Oak Ridge, TN 37831, USA*

<sup>4</sup>*National Superconducting Cyclotron Laboratory, Michigan State University, East Lansing, MI 48824, USA*

<sup>5</sup>*Institute of Nuclear Physics PAN, 31-342 Cracow, Poland*

<sup>6</sup>*Joint Institute for Nuclear Research, 141980 Dubna, Moscow Region, Russia*

<sup>7</sup>*Department of Chemistry, Michigan State University, East Lansing, MI 48824, USA*

(Dated: June 10, 2021)

Results of decay spectroscopy on nuclei in vicinity of the doubly magic  $^{48}\text{Ni}$  are presented. The measurements were performed with a Time Projection Chamber with optical readout which records tracks of ions and protons in the gaseous volume. Six decays of  $^{48}\text{Ni}$ , including four events of two-proton ground-state radioactivity were recorded. An advanced reconstruction procedure yielded the 2p decay energy for  $^{48}\text{Ni}$  of  $Q_{2p} = 1.29(4)$  MeV. In addition, the energy spectra of  $\beta$ -delayed protons emitted in the decays of  $^{44}\text{Cr}$  and  $^{46}\text{Fe}$ , as well as half-lives and branching ratios were determined. The results were found to be consistent with the previous measurements made with Si detectors. A new proton line in the decay of  $^{44}\text{Cr}$  corresponding to the decay energy of 760 keV is reported. The first evidence for the  $\beta 2p$  decay of  $^{46}\text{Fe}$ , based on one clear event, is shown.

PACS numbers: 23.50.+z, 23.90.+w, 27.40.+z, 29.40.Cs, 29.40.Gx

## I. INTRODUCTION

The quest to reach the limits of nuclear existence and to learn properties of nuclides at these limits is one of most important topics in the present-day low-energy nuclear physics. The progress in this field is largely driven by recent advances of experimental techniques allowing efficient production, separation and detection of very exotic nuclei, located far from the  $\beta$  stability and characterized by extreme proton-to-neutron imbalance. Although the neutron-deficient side of the nuclidic chart is much better explored than the neutron-rich frontier, there are still a lot of unsurveyed areas on this chart and open questions concerning nuclei at and beyond the proton drip-line. The nuclear properties in this region are shaped by the interplay between large  $\beta$ -decay  $Q$  values, low or negative proton separation energies, and the confining effects of the Coulomb barrier. The resulting characteristic phenomena include a variety of  $\beta$ -delayed particle emission channels, proton radioactivity and two-proton radioactivity [1–4].

The latter process, discovered 12 years ago [5, 6] is still not well known. Its mechanism is not fully understood and its potential to reveal nuclear-structure information is not firmly established yet. Up to now, the simultaneous two-proton (2p) emission from the ground state was unambiguously observed in  $^6\text{Be}$ ,  $^{19}\text{Mg}$ ,  $^{45}\text{Fe}$ ,  $^{48}\text{Ni}$ , and  $^{54}\text{Zn}$  [1]. It is expected, however, that this decay mode

should be observable for almost every even- $Z$  element up to tellurium [7]. In the first experiments the evidence for 2p decay was obtained by means of arrays of Si detectors which only allowed for a determination of the total decay energy and the decay time [5, 6, 8]. To fully explore the physical information carried by the two protons, however, one has to record their momenta separately. This requirement led to the development of new types of detectors capable of recording tracks of charged particles in a gaseous medium, based on the Time Projection Chamber (TPC) principle. One such device [9] provided the first direct evidence for the 2p decay of  $^{45}\text{Fe}$  [10] and  $^{54}\text{Zn}$  [11]. In another detector, developed at the University of Warsaw, a novel concept of optical readout was applied to a drift chamber which led to the Optical Time Projection Chamber (OTPC) [12]. The OTPC detector was successfully used to measure the first full proton-proton correlation picture for the 2p decay of  $^{45}\text{Fe}$  [13, 14]. This experiment revealed the three-body character of the process and provided the first evidence for the sensitivity of the 2p correlation pattern to the angular momentum composition of the initial wave function. In addition, the OTPC detector was instrumental in the discovery of the  $\beta$ -delayed three-proton ( $\beta 3p$ ) emission in the case of  $^{45}\text{Fe}$  [15] and  $^{43}\text{Cr}$  [16].

Recently, the OTPC detector was used to study the decay of the extremely neutron-deficient ( $T_z = -4$ ) and presumably doubly-magic  $^{48}\text{Ni}$ . The main result of this work was the first observation of the 2p decay of  $^{48}\text{Ni}$ . The preliminary results on the decay of  $^{48}\text{Ni}$  were published in Refs. [17–19]. Here we present the results of the full and final analysis of this experiment. An improved

\* pfutzner@fuw.edu.pl

track reconstruction procedure was used to accurately determine the energies of the detected particles. In addition to the 2p decay of  $^{48}\text{Ni}$ , the  $\beta$ -delayed protons emitted in the decays of  $^{46}\text{Fe}$  and  $^{44}\text{Cr}$  were recorded. Decays of both these nuclei were studied before by means of implantation in a stack of Si-detectors by Dossat et al. [20]. The comparison of our data with those from Ref. [20] provides a consistency check for our algorithms of the data analysis. It is used also to point out advantages of the TPC technique over Si detectors in the charged particle spectroscopy of exotic nuclei, especially in detecting low-energy protons. Such comparison demonstrates the complementarity of both techniques.

Section II of this paper presents the experimental details concerning the production, separation, and in-flight identification of the ions of interest. The OTPC system is described with the focus on modifications and improvements with respect to the detector used in the 2p spectroscopy of  $^{45}\text{Fe}$  [13, 14]. In Sec. III the main steps of the data analysis are presented, in particular the procedure for the proton track reconstruction. The main results are listed and discussed in Sec. IV which is followed by conclusions in Sec. V.

## II. EXPERIMENTAL TECHNIQUE

### A. Production and identification of ions

The experiment was carried out at the National Superconducting Cyclotron Laboratory (NSCL). The ions were produced in a fragmentation reaction by bombarding a  $580\text{ mg/cm}^2$  natural nickel target with a  $^{58}\text{Ni}$  beam with an energy of  $160\text{ MeV/nucleon}$ . A rotating target assembly was developed for this experiment by Oak Ridge National Laboratory and the University of Tennessee. In the course of the experiment the target was run at speeds up to  $900\text{ RPM}$  and withstood beam currents up to  $40\text{ pA}$ . The ions of interest were separated from contaminants using the A1900 fragment separator [21] in the achromatic setting with two aluminum degraders mounted in the I1 and I2 focal planes. The degraders had thickness of  $193\text{ mg/cm}^2$  and  $302\text{ mg/cm}^2$ , respectively. Selected ions were transferred to the S2 vault where the OTPC detector system was placed. The average time of flight of ions from the target to the detector, calculated with the LISE code [22], was about  $500\text{ ns}$ .

Each fragment arriving at the detector was identified using the time-of-flight and energy-loss technique. The time-of-flight (TOF) was measured between a plastic scintillator, positioned at the middle focal plane of the A1900 separator, and a Si detector placed at the end of the beam line just before the OTPC detector. This Si detector also provided the energy loss ( $\Delta E$ ) data. The average rate of ions at detector setup in the S2 vault was about  $10\text{ ions/s}$ . The complete data were recorded by the standard acquisition system of the A1900 separator. The resulting identification plot is presented in Fig. 1.

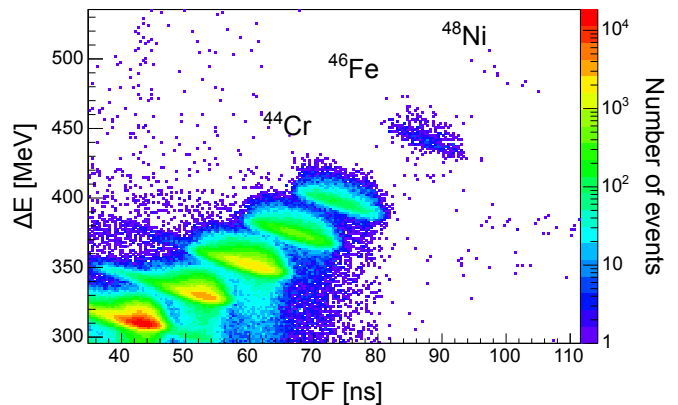


FIG. 1. (Color on-line) The identification spectrum of all ions arriving to the S2 vault, as collected by the A1900 standard acquisition system.

### B. The OTPC detection system

The Optical Time Projection Chamber (OTPC) was developed at the University of Warsaw specifically to study very rare decay modes with emission of charged particles, like 2p radioactivity. The main concept and some details of the unit used in the study of  $^{45}\text{Fe}$  were given in Ref. [12, 14]. For the present experiment a new chamber was designed and produced. Here we briefly summarize its main features.

The detector is schematically shown in Fig. 2. The active volume, having dimensions of  $33 \times 20 \times 14.2\text{ cm}^3$  (depth, width and height, respectively), is filled with a gaseous mixture at atmospheric pressure. In this study a gas mixture of 49.5% Ar, 49.5% He, and 1%  $\text{N}_2$  was used.

Within the active volume, between the cathode and the amplification stage, a constant and uniform electric field is maintained with the help of copper electrodes spaced evenly on the side walls. The direction of this field is vertical and its strength was about  $E = 210\text{ V/cm}$ .

The incoming ions enter the active volume horizontally through a kapton entrance window. If the ion is stopped inside the active volume, its decay with emission of heavy charged particles, like protons or  $\alpha$  particles, can be registered. Primary electrons, resulting from the gas ionization by the stopping ion and by emitted charged particles, drift with the constant velocity  $v_d$  toward the amplification stage, passing through the gating electrode. We note that electrons emitted during  $\beta$  decays generate ionization too weak to be registered by the detector. In order to allow for the registration of both the implanted ion and the particles emitted in the decay, a gating electrode connected to a fast-switching high-voltage power supply was used. By changing the potential of this electrode, we could either block most of the primary ionization electrons or let them pass to the amplification section. These settings are referred to as the "low sensitivity" and "high sensitivity" regimes,

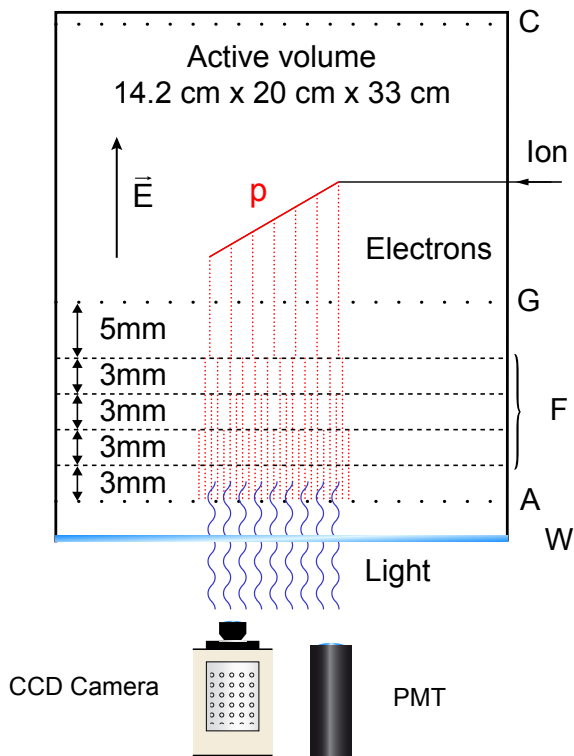


FIG. 2. (Color on-line) Schematic view of the OTPC chamber with an example event of  $\beta$ -delayed proton emission from a stopped ion. Only ionization electrons resulting from the proton are marked. The letters on the right indicate: C - cathode, G - gating electrode, F - set of 4 GEM foils, A - wire-mesh anode, W - window transparent to visible light.

respectively. Switching between these two settings takes about  $100\mu\text{s}$ .

The signal amplification is performed using four Gas Electron Multiplier foils (GEM) [23]. The voltage between the two sides of each foil and the voltage between the neighboring foils can be controlled individually, in order to optimize the performance of the system. The former were set in the range between 240 and 280 volts and were tuned during the experiment in order to maintain maximum possible gain. The voltages between GEM foils were set to 800 V. Between the last GEM foil and the final anode electrode a high voltage of 1000 V was supplied, causing electrons to stimulate light emission from particles of the gas mixture. At this point the electric signal is converted to light.

This light is registered with a digital camera (CCD) and a photomultiplier (PMT) connected to an oscilloscope. In this experiment a  $512 \times 512$  16 bit pixel back-thinned CCD camera (Hamamatsu c9100-13) and a 100 MS/s 14 bit per sample oscilloscope (NI PXI-5142) were used. The CCD image represents a projection of an event on the plane of GEM foils, integrated over exposure time (typically around 30 ms). The PMT trace provides the total light intensity as a function of time, which allows for a determination of the time between the implantation

and the decay. In addition, the PMT signal contains the information of the event along the direction of the electric field, i.e. perpendicular to the anode plane. Moreover, if the entire track of an emitted proton is contained within the active volume, it can be reconstructed in 3D by combining data from the PMT and the CCD.

The chamber used in this experiment differs in a few key aspects from the detector used in the study of  $^{45}\text{Fe}$  and described in Ref. [12]. First, the ions enter the detection volume perpendicularly to the electric field and not diagonally, as before. Thus, contrary to the previous case, the distance of the stopped ion to the amplification stage does not depend on the implantation depth. Even more important is that the ions do not penetrate the amplification section, which could cause malfunctions due to large ionization. Second, the wire-mesh electrodes were replaced by the GEM foils which reached the same amplification with smaller voltages applied and resulted in much more stable working conditions. The effects of electric discharges, which blocked the previous detector are now practically absent. Finally, we use a new CCD camera with a better quantum efficiency.

In order to optimize the implantation depth of the ions of interest, an adjustable degrader was placed in front of the OTPC entrance window. In this experiment an  $832\mu\text{m}$  thick Al degrader was used. However, due to the large energy spread of ions coming from the A1900 separator, only about 65% of  $^{48}\text{Ni}$  ions could be stopped in the active volume of the OTPC, the rest either punched through the chamber or stopped in the entrance window or before.

The OTPC acquisition system was triggered selectively, based on the  $\Delta E$ -TOF information for the incoming ion. The trigger signal was activated only by ions for which both the TOF and the  $\Delta E$  values exceeded certain limits. Those limits were adjusted to accept all ions of  $^{48}\text{Ni}$  and of  $^{46}\text{Fe}$ , and a small part of  $^{44}\text{Cr}$  ions. During the entire experiment a special "extended exposure" mode of operation was used. In this mode, while awaiting the trigger, the OTPC is kept in the "low sensitivity" regime and the CCD camera is continuously taking images with a constant exposure time (referred to as the "implantation gate"). These images are discarded unless a trigger signal arrives during the exposure. Upon the arrival of the trigger the OTPC is switched to the "high sensitivity" regime and the CCD exposure is extended by a fixed time period (referred to as the "decay gate"). At the same moment the primary beam is stopped to prevent other ions from entering the detector in the high sensitivity mode. The signal waveform from the PMT is stored in a circular buffer of the digital oscilloscope. The trigger determines the time span of the recorded waveform. It starts one length of the implantation gate before the trigger and spans over the entire exposure time until the end of the decay gate. This sequence of events is shown in Fig. 3.

During the experiment the implantation gate was set to 32 ms at all times. The decay gate was set to 32 ms for

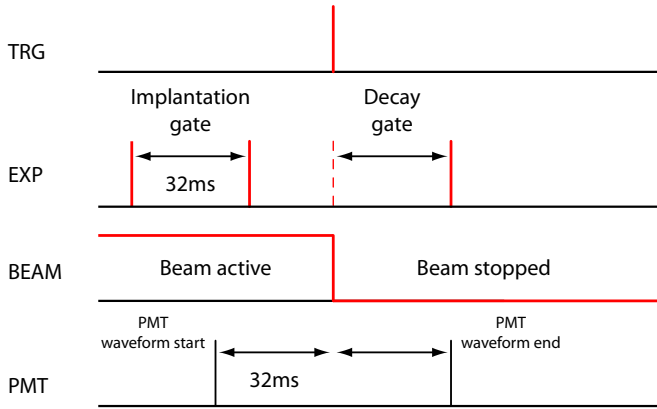


FIG. 3. The sequence of events in the extended exposition mode of the OTPC operation. TRG shows the arrival time of an ion of interest, EXP marks exposures of the CCD camera, BEAM indicates the stopping of the primary beam, while PMT shows the range of the registered waveform from the photomultiplier.

most of the time, however, some data were taken with a longer decay gate of 120 ms. These settings are referred to as the short and the long exposure, respectively. The PMT signal was sampled with 50 MHz and 25 MHz for events taken in the short and long exposure mode, respectively. The CCD camera used in this experiment could not accept a trigger for  $780 \mu\text{s}$  after each implantation exposure. This introduced a dead time of 2.4% and 0.6% in the short and long exposure settings, respectively.

For each event the ID information for the triggering ion was recorded. The  $\Delta E$  signal from the Si detector, pre-amplified and processed by a fast amplifier, and the delayed signal from the time-to-amplitude converter (TAC) representing the TOF of the ion, were combined by means of a linear summing module. Then this signal was fed to a second channel of the oscilloscope which recorded its full waveform. After the decay gate was closed, all collected data, comprising the CCD image, the waveform of the PMT signal, and the waveform of the ID signals were read and stored on a disk. Since the primary beam was switched-off for a period of about 1 s after the trigger, there was ample time for data read-out and storage before the beam was switched on again and the OTPC was ready for another trigger. Example data recorded for one event are displayed in Fig.4.

### III. DATA ANALYSIS

#### A. Ion identification

From the ID information of each recorded event (Fig. 4c) the identification spectrum of all ions which triggered the OTPC system was constructed. By fitting the shape of the signals with help of the Levenberg-Marquardt algorithm, as implemented in the levmar 2.5 library [24],

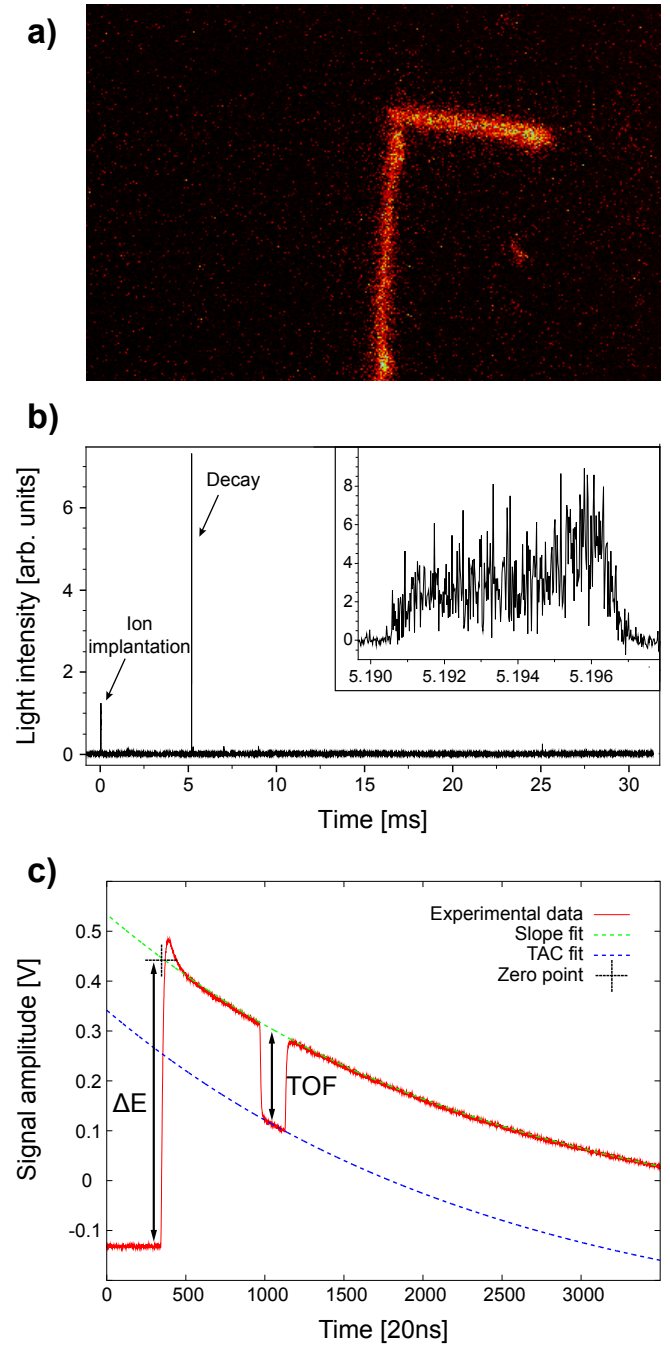


FIG. 4. (Color on-line) An example set of data recorded by the OTPC detector for one event of  $\beta$ -delayed proton emission from  $^{46}\text{Fe}$ . a) On the CCD image a track of an ion coming from below and a track of a proton emitted about 5 ms later are visible; b) The waveform of the PMT signal shows the sequence of events and the zoomed decay part in the insert; c) the ID information for the ion consists of the signal from the Si detector and the superimposed signal from the TAC. The fitted curves used to extract the corresponding values of the  $\Delta E$  and the TOF are also shown.

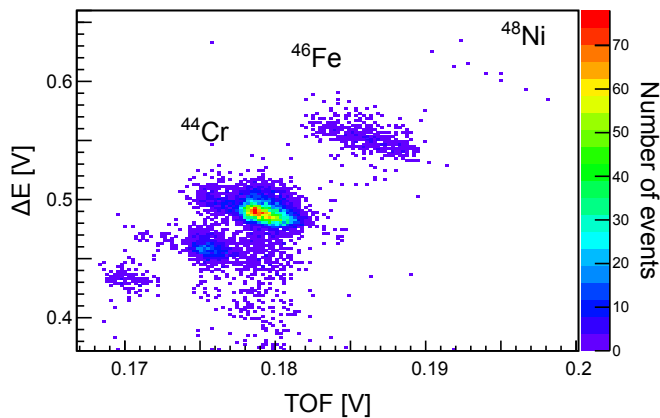


FIG. 5. (Color on-line) The identification spectrum extracted from the ID data recorded by the OTPC showing all ions which triggered the OTPC acquisition system.

the relevant physical parameters were extracted. First, from the exponential slope of the Si signal its amplitude and thus the value of the  $\Delta E$  was determined. Then, taking this slope into account, the amplitude of the TAC signal was found yielding the value of the TOF. The resulting ID spectrum for all recorded events is presented in Fig. 5.

In total 8580 events were collected, 6563 were taken with the short exposure and 2017 with the long exposure time. We identify 9 events of  $^{48}\text{Ni}$ , 471 events  $^{46}\text{Fe}$  and 5542 events of  $^{44}\text{Cr}$ .

An inspection of Fig.1 reveals that the A1900 acquisition system recorded 10 events of  $^{48}\text{Ni}$ , thus one more than the OTPC system. The A1900 system was taking data independently of the status of the OTPC. This one event could have been missed by the OTPC acquisition either due to the CCD camera induced dead-time or if it arrived when the OTPC was not collecting data, for example during adjustments of the OTPC.

## B. Track reconstruction

When a charged particle emitted in a decay is stopped inside the active volume of the OTPC, the recorded data allows for a determination of the energy and the direction of the particle's track in the 3D space. The procedure which we developed for such a reconstruction is based essentially on comparison of the observed track with simulations.

First, the regions from the CCD image and the PMT waveform which contain the signal from the particle are cut out yielding two experimental distributions for further processing. Since the ratio between the energy deposited by a particle in the gas and the registered amount of light was not perfectly stable, we analyze only the shape of the distributions, ignoring the absolute amplitude. Therefore, both distributions are normalized to yield the integral of 1. In addition they are smoothed

with a gaussian filter to reduce high frequency noise. The parameters of this filter were kept constant and the same for all events.

We assume that the measured signal, both in the CCD image and in the PMT waveform, is proportional to the primary ionization density which in turn is proportional to the stopping power,  $dE/dx$ , of the charged particle. Using the SRIM2013 code [25] we calculate the stopping power profile along the trajectory of the particle in the OTPC gas mixture for a given initial energy of the particle. Further, for an assumed particle emission angle, we project the calculated energy-loss profile on the anode plane (horizontal) and on the direction perpendicular to it (vertical). The length scale of the vertical profile is expressed in the units of time assuming the constant drift velocity  $v_d$  of electrons in the OTPC chamber. To account for the diffusion of the drifting charge, we introduce a spread to the projected profiles by a gaussian function. The widths characterizing the diffusion in the horizontal and the vertical directions can be different. Finally, both simulated profiles are smoothed in the same way as the experimental distributions and normalized to the unit integral. The two profiles thus produced can be compared with the experimental distributions.

To quantify the comparison of the simulated CCD response with the corresponding experimental distribution we introduce the function:

$$\xi_{CCD}^2 = \sum_{i,j} [CCD_{exp}(i,j) - CCD_{sim}(i,j)]^2, \quad (1)$$

where  $CCD_{exp}(i,j)$  and  $CCD_{sim}(i,j)$  are the smoothed, normalized experimental signal, and the simulated OTPC's response for the pixel coordinates  $i,j$ , respectively. The summing runs over all pixels of the experimental distribution. Similarly, for the PMT signal we define:

$$\xi_{PMT}^2 = \sum_i [PMT_{exp}(i) - PMT_{sim}(i)]^2, \quad (2)$$

where  $PMT_{exp}(i)$  and  $PMT_{sim}(i)$  are the  $i^{th}$  element of the experimental and the simulated PMT signal, respectively. Again the summing range covers the whole signal. Finally, we combine both functions:

$$\xi_{tot}^2 = \frac{\xi_{CCD}^2}{w_{CCD}} + \frac{\xi_{PMT}^2}{w_{PMT}}, \quad (3)$$

where  $w_{CCD}$  and  $w_{PMT}$  are the weighting factors reflecting the corresponding number of degrees of freedom. For the  $w_{CCD}$  we take the length of the track on the CCD image in pixels, and for the  $w_{PMT}$  we take the number of samples in the PMT waveform. The reconstruction of the particle track is done by running the simulations for various values of the initial energy, emission angles and the two diffusion widths, to find the set of parameters which minimizes the function  $\xi_{tot}^2$ . To illustrate this procedure, the reconstruction results for the event shown in Fig. 4 are shown in Figs. 6 and 7.



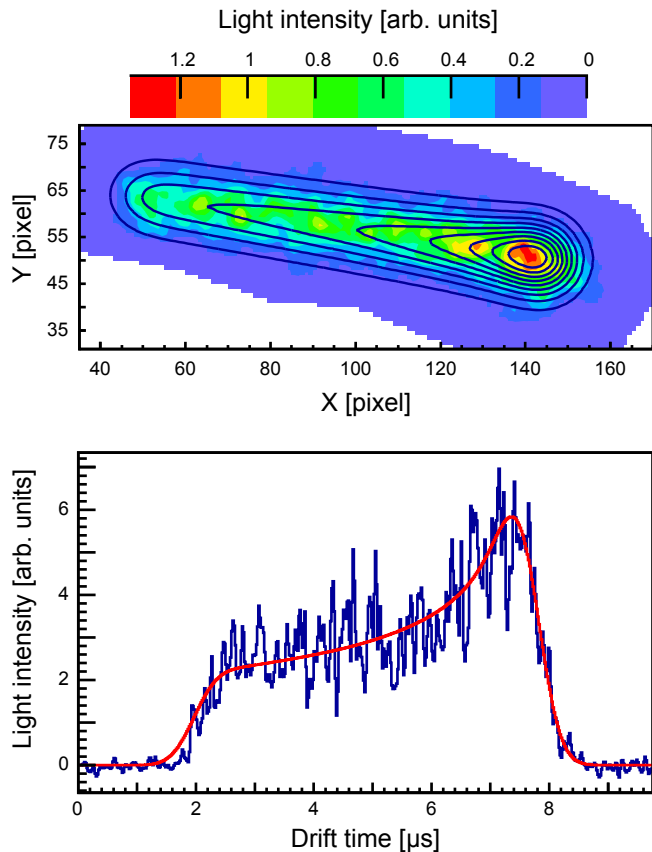


FIG. 6. (Color on-line) Reconstruction of a  $\beta$ -delayed proton track from the event shown in Fig. 4. The best fitting simulation is indicated by the contour lines on the CCD image (top) and by the red line on the PMT waveform (bottom).

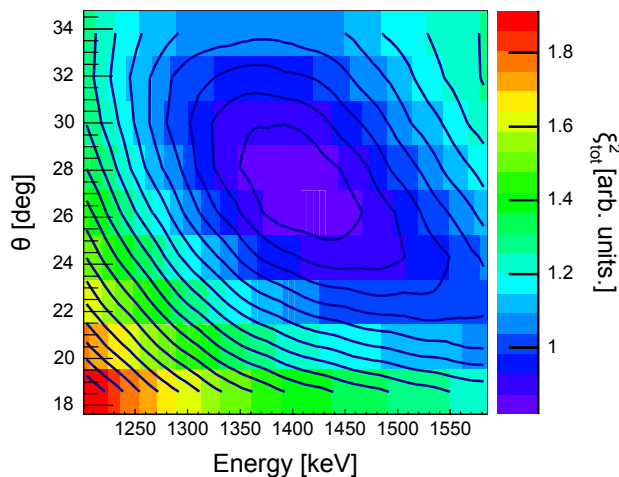


FIG. 7. (Color on-line) The map of  $\xi_{tot}^2$  values around the minimum value for the event shown in Fig. 4 plotted as a function of the proton energy and the angle  $\theta$  between the proton's track and the horizontal plane. Each point represents the value minimized over all parameters except the energy and  $\theta$ .

The events with the simultaneous emission of two protons were reconstructed using the same procedure. To simulate the detector response for such an event, first each proton was simulated individually. Then, both simulations were merged assuming that the emission originated from same place and occurred the same time. In cases where it was not clear which part of the PMT signal corresponds to which track on the CCD image, all possible configurations were simulated and the one providing the least  $\xi_{tot}^2$  was chosen.

### C. Energy calibration using $^{44}\text{Cr}$

To verify the reconstruction procedure and to fine-tune the value of the electron drift velocity  $v_d$ , the  $\beta$ -delayed protons emitted in the decay of  $^{44}\text{Cr}$  were used. The spectrum of delayed protons for this case was measured by Dossat et al. [20]. We were able to reconstruct 103 tracks of protons originating from  $^{44}\text{Cr}$  which were fully confined in the OTPC active volume. The resulting energy spectrum, see Fig. 8, clearly shows pronounced peaks. Two lines, marked in Fig. 8 as 2 and 3, correspond to the lines found in Ref. [20] at 908 keV and 1384 keV, respectively. Taking into account that we are extracting the kinetic energy of the proton while results of Ref. [20] refer to the decay energy which includes the recoil of the daughter nucleus, we do reproduce these energy values with the drift velocity of  $v_d = 6.00(25)$  mm/ $\mu\text{s}$  which fixes the energy calibration. The results for the decay of  $^{44}\text{Cr}$  will be discussed in more detail in Sec. IV A.

### D. Uncertainties

The final uncertainties of the reconstruction procedure were estimated by combining the inaccuracy of the  $\xi^2$  minimization, and the systematic error of the drift velocity. The total uncertainty of proton energy was found to range from 4% to 8%. The angle  $\theta$  of a proton track with respect to the horizontal plane is determined with an accuracy of about  $4^\circ$ . For the event shown in Fig. 4 the reconstruction procedure yielded the proton kinetic energy  $E_p = 1393(50)(6)$  keV and the track angle with respect to the horizontal plane  $\theta = 28^\circ(4^\circ)(1^\circ)$ , where the first error corresponds to the statistical uncertainty of the  $\xi^2$  minimization and the second error reflects the systematic uncertainty of the drift velocity.

## IV. RESULTS

### A. $^{44}\text{Cr}$

#### 1. Half-life and the total branching ratio

Out of 5542 ions identified as  $^{44}\text{Cr}$  by the OTPC ID procedure, 4098 were stopped well inside the active vol-

ume of the chamber at a sufficient distance from the walls to ensure that the emission of a delayed proton is clearly visible. In 183 events such an emission indeed was observed. Although in many cases the emitted proton escaped the OTPC volume, this number together with the number of well implanted ions allows for the determination of the half-life and the total branching ratio for the  $\beta$ -delayed proton emission.

To extract the half-life of  $^{44}\text{Cr}$  the maximum likelihood method was used combining events registered with both the short and the long exposure. Following the procedure described in Ref. [16] the half-life was found to be  $T_{1/2} = 25_{-4}^{+6}$  ms. The reason for the large error bars is that most of the events were collected in the short exposure mode, with the decay gate of 32 ms being of the same order as the measured half-life. This result agrees within  $3\sigma$  with the value reported by Dossat et al. of  $T_{1/2} = (43 \pm 2)$  ms [20].

In the analysis of the branching ratio one has to take into account the fact that the  $\beta$  particles are not observed in the OTPC. Thus, an event picturing only the implanted ion indicates that either no decay occurred within the observation time (decay gate) or the  $\beta$  decay did occur but without emission of delayed protons. Since the half-life and the length of the decay gate are known, the maximum likelihood method can be used to determine the branching ratio in such case [16]. Using the more precise half-life value measured by Dossat et al. we found that the total branching ratio for the  $\beta$ -delayed proton emission by  $^{44}\text{Cr}$  is  $b_{\beta p} = 10(1)\%$ . This is to be compared with the value reported by Dossat et al. of  $14.0(9)\%$  [20]. We note that our method is essentially based on counting the incoming ions and the decay events, and its ultimate accuracy is limited only by statistics. In particular, it is free of systematical errors present in the method used by Dossat et al. [20], who had to impose an arbitrary cut on the proton energy spectrum to avoid the significant background due to  $\beta$  particles. In addition, our method does not suffer from the uncertainty of normalization. The relative uncertainty of our result is of the same order as that of Ref. [20] but the decay gate in our measurement was not optimized for the decay of  $^{44}\text{Cr}$  and the number of collected ions of  $^{44}\text{Cr}$  in our experiment was smaller by an order of magnitude.

## 2. Energy spectrum

Using the procedure described in Sec. IIIB, we have reconstructed all events of  $\beta p$  emission in which the full proton track was recorded. In total, 103 decay events of  $^{44}\text{Cr}$  could be successfully reconstructed and the energy spectrum of the emitted protons is shown in Fig. 8.

The three broad structures seen in this Figure (marked as 2, 3, and 4) correspond to the peaks reported by Dossat et al. [20] at the decay energy of 908 keV, 1384 keV, and 1741 keV, respectively. The widths of these peaks are

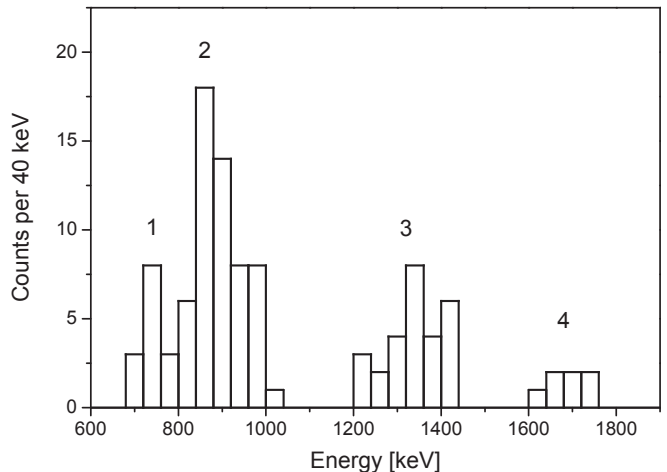


FIG. 8. Energy spectrum of  $\beta$ -delayed protons emitted from  $^{44}\text{Cr}$  with four lines marked.

TABLE I. Energies of proton groups observed in the decay of  $^{44}\text{Cr}$  and the corresponding branching ratios. The  $E_p$  denotes the proton kinetic energy. The values for Ref. [20] were recalculated from published decay energy values by correcting for the daughter recoil.

	This work		Ref. [20]	
	$E_p$ [keV]	$I_p$ [%]	$E_p$ [keV]	$I_p$ [%]
1	742(24)(10) <sup>a</sup>	0.6(2)		
2	896(53) <sup>b</sup>	2.7(5)	887(11)	1.7(3)
3	1340(62) <sup>b</sup>	1.4(3)	1353(12)	1.1(3)
4	1680(44) <sup>b</sup>	0.5(2)	1700(15)	0.6(3)

<sup>a</sup> The first error comes from the minimization procedure, while the second reflects the uncertainty of the drift velocity.

<sup>b</sup> The energy value calculated as the average of events in the peak area and the error corresponds to the standard deviation of this average.

larger than the energy resolution, both in Ref. [20] and in this work, indicating that they are composed of overlapping lines. In addition, our spectrum shows a narrow structure at 742 keV (marked as 1 in Fig. 8), consistent with a single proton line. This line has not been identified by Dossat et al. probably because of the large  $\beta$  background, see Fig. 15b of Ref. [20]. This illustrates the advantage of the OTPC detector which is not sensitive to  $\beta$  particles.

On the other hand, due to the limited active volume, protons of high energy escape the OTPC detector which presents a disadvantage if compared to an array of Si detectors. While most of the protons at 1000 keV are fully stopped inside the OTPC, the probability to escape strongly increases with the proton energy. At the energy of 1800 keV, the length of the proton track in the OTPC gas mixture is about 11 cm, thus many such protons escape the active volume and cannot be reconstructed. That is why at about 1700 keV (peak 4 in

Fig. 8) we see only a part of the real intensity. To correct for this effect we determined the efficiency of stopping the entire proton track within the fiducial volume of the detector as a function of proton energy by a Monte Carlo method. The ranges of protons in the OTPC gas mixture were calculated by the SRIM2013 code [25], the measured implantation profile of  $^{44}\text{Cr}$  ions in the gas volume was taken into account, and the isotropic emission of  $\beta$ -delayed protons was assumed. Taking the total proton branching ratio and the number of counts from Fig. 8, and correcting for the stopping efficiency, we have obtained the branching ratios for individual peaks. They are presented in Table I in comparison with results of Ref. [20]. As long as emitted protons are stopped within the OTPC, our method provides more accurate values of the branching ratios as the spectrum is not affected by the background of  $\beta$  particles.

## B. $^{46}\text{Fe}$

### 1. Production cross-section

Although the ion-optical setting of the A1900 separator was not optimal for  $^{46}\text{Fe}$ , the transmission of this nucleus was large enough for the determination of the production cross section. According to the procedure described in Ref. [26], the cross-section is given by:

$$\sigma = \frac{N_{Fe}}{N_{proj}} \frac{A_t}{N_A d_t} \frac{1}{T_1 T_2}, \quad (4)$$

where  $N_{proj}$  and  $N_{Fe}$  is the number of beam particles which hit the target and the number of  $^{46}\text{Fe}$  ions identified, respectively,  $A_t$  is the molar mass of the target,  $N_A$  is the Avogadro number,  $d_t$  is the target thickness in  $\text{g}/\text{cm}^2$ ,  $T_1$  is the transmission of  $^{46}\text{Fe}$  from the target to the final focus of the A1900 separator, which takes into account losses in the material of the target and in the degraders, and  $T_2$  represents the transmission from the A1900 final focus through the beam line to the Si detector.

We use the number of identified ions,  $N_{Fe}$ , from the A1900 standard identification system (see Fig. 1) which does not suffer any dead-time limitations. We found  $N_{Fe} = 503$ , while the number of projectiles,  $N_{proj}$ , was determined by a Faraday cup to be  $N_{proj} = 8 \times 10^{16}$ . The target of  $d_t = 580 \text{ mg}/\text{cm}^2$  thickness was made of natural nickel with  $A_t = 58.7 \text{ g}$ . The transmission  $T_1$  was calculated by LISE++ code [22] using the momentum distribution according to the model of Morrissey [27], which yielded  $T_1 = 0.13(6)$ . The large uncertainty of this value is dominated by the uncertainty of the shape of the momentum distribution. It was estimated by comparing predictions of different models of this distribution [22]. The transmission  $T_2$  was determined experimentally to be  $T_2 = 0.40(5)$ . Finally, the production cross section for  $^{46}\text{Fe}$  in the fragmentation reaction of

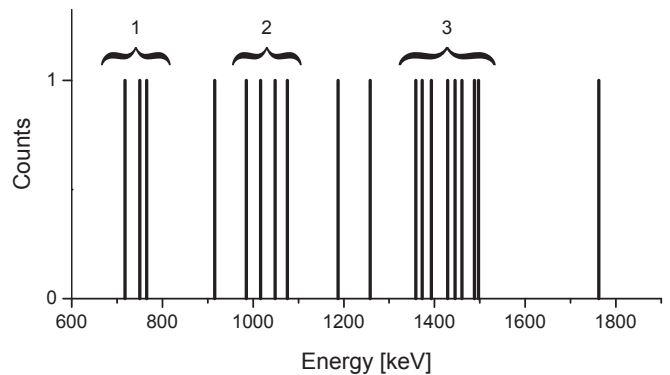


FIG. 9. Energy spectrum of  $\beta$ -delayed protons emitted from  $^{46}\text{Fe}$ .

$^{58}\text{Ni}$  beam at 160 MeV/nucleon on a natural nickel target is  $\sigma = (25 \pm 12) \text{ pb}$ . This number is fairly well reproduced by the EPAX 3 parametrization which predicts  $\sigma^{EPAX} = 14 \text{ pb}$  [28].

### 2. Half-life and the total branching ratio

In the OTPC identification spectrum 471 events of  $^{46}\text{Fe}$  were found. Out of this number 269 ions were stopped well inside the chamber, far enough from the walls to see the eventual emission of  $\beta$ -delayed particles. In 139 events such emission was observed, which allows for the determination of the half-life and the total branching ratio for  $\beta$ -delayed proton emission.

Using the maximum likelihood method we found that the half-life of  $^{46}\text{Fe}$  is  $T_{1/2} = 16.4^{+4.2}_{-2.8} \text{ ms}$ , which is consistent with the value of  $T_{1/2} = 13.0(17) \text{ ms}$  reported by Dossat et al. [20]. By combining these two values according to the procedure described in Ref. [29] we obtain the more accurate result of  $T_{1/2} = 14.0^{+1.4}_{-1.3} \text{ ms}$ .

Using this combined value of the half-life and following the same procedure as for  $^{44}\text{Cr}$  (sec. IV.A.1), the total branching ratio for the emission of  $\beta$ -delayed protons in the decay of  $^{46}\text{Fe}$  is found to be  $b_{\beta p} = 66(4)\%$ . This result agrees within  $3\sigma$  with the value of  $b_{\beta p} = 79(4)\%$  obtained by Dossat et al. [20]. Our result does not suffer from any systematical uncertainties due to the  $\beta$  background.

### 3. Energy spectrum

In most cases the  $\beta$ -delayed protons had energy large enough to escape from the chamber. However, 19 such events could be reconstructed. The resulting energy spectrum is shown in Fig. 9.

Despite the low statistics, there are indications of three lines in the spectrum. The line located at about 1400 keV (marked as 3) is compatible with the line at 1457(28) keV reported by Dossat et al. [20] which corresponds to the proton kinetic energy of 1425 keV. The number of counts



in this line, corrected by the stopping efficiency of protons, corresponds to the branching ratio of 3.6(13)%. In Ref. [20] this line was assigned the branching of 10(3)%. Other proton lines observed in Ref. [20] had larger energies, in fact too large to be reconstructed in the present experiment. On the other hand, we do see traces of two lines at lower energies (750 keV and 1050 keV) which were not seen by Dossat et al. The corresponding branching ratios are 1.2(7)% and 1.6(8)%, respectively. In general the OTPC is more sensitive for low energy particles than silicon detectors, mainly due to lack of  $\beta$  background.

#### 4. $\beta 2p$ decay of $^{46}\text{Fe}$

Among the observed decay events of  $^{46}\text{Fe}$ , there is one clearly showing the simultaneous emission of two high-energy protons. This event, presented in Fig.10, provides the first evidence for  $\beta$ -delayed two-proton emission from this nucleus. Unfortunately, both protons left the active volume of the OTPC so their energies could not be reconstructed. From the visible length of both tracks, however, we can determine the lower limits of their energies. The real length of the two tracks was evidently larger than 99 mm and 129 mm which for the protons in the OTPC gas mixture corresponds to an energy larger than 1.67 MeV and 1.96 MeV, respectively. Thus the energy difference between the proton emitting excited state in  $^{46}\text{Mn}$  and the final state in the  $\beta 2p$  daughter  $^{44}\text{V}$  must have been larger than 3.63 MeV. Taking the  $^{44}\text{V}$  mass excess value  $\Delta m = -24.12$  MeV [30] and the mass excess of the Isobaric Analog State (IAS) of  $^{46}\text{Fe}$  in  $^{46}\text{Mn}$  as  $\Delta m = -7.473$  MeV [20] we obtain the energy difference between these two states of 2.07 MeV. This means that the two-proton emission proceeded from a state located more than 1.56 MeV above the IAS state. One  $\beta 2p$  event corresponds to the branching ratio of 0.4(6)%. This nicely illustrates the extreme sensitivity of the OTPC detector - one clearly resolved event is sufficient to claim the observation of a new decay mode.

### C. $^{48}\text{Ni}$

#### 1. Production cross-section

Using the same procedure as in the case of  $^{46}\text{Fe}$  (Eq. 4), we can determine the production cross section for  $^{48}\text{Ni}$ . For the number of identified ions we use 10, as given by the A1900 ID system, see Fig.1. The transmission to the final focus of the A1900,  $T_1$ , was calculated using the LISE++ code [22] according to the procedure described in Ref.[31], which yielded  $T_1 = 0.34(3)$ . The remaining values were the same as in the case of  $^{46}\text{Fe}$ . The resulting cross section for the production of  $^{48}\text{Ni}$  in the fragmentation reaction of a  $^{58}\text{Ni}$  beam at 160 MeV/nucleon on a natural nickel target is  $\sigma = (150 \pm 50)$  fb.

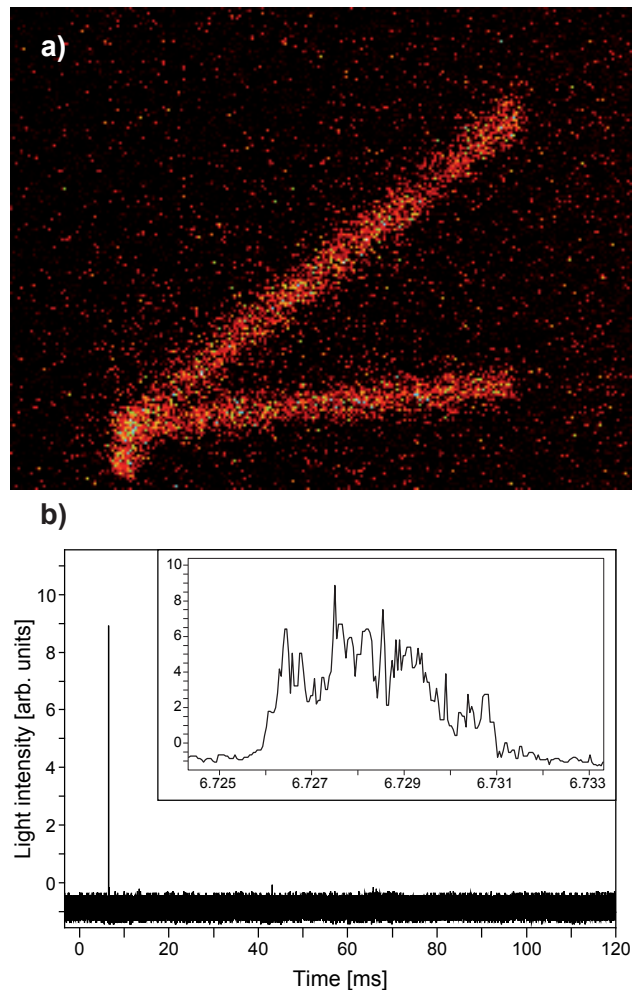


FIG. 10. Decay event showing the  $\beta 2p$  emission from  $^{46}\text{Fe}$ . On the CCD image (a) a short track of the ion entering the chamber from below and two long tracks of particles leaving the detector volume are visible. The corresponding PMT waveform (b) proves that both particles were emitted at the same time. Since the ion of  $^{46}\text{Fe}$  stopped very close to the entrance window, the signal from the implantation, at the zero time, was too small to be visible in this scale. In the insert the zoomed decay part of the waveform is shown.

In the previous work we had reported the value of  $\sigma = (100 \pm 30)$  fb [18]. The difference arises solely from the  $T_1$  coefficient. In Ref. [18] it was estimated by using the analytical prediction of LISE++ and the momentum distribution of Ref. [32]. Here, we use the more realistic Monte Carlo version of LISE++ and the momentum distribution given by the Morrissey model [27], as recommended by Tarasov et al. [31]. The comparison of our result with the literature and with the predictions of the EPAX models is given in Table II.

TABLE II. Production cross-section for  $^{48}\text{Ni}$  in the reaction of a  $^{58}\text{Ni}$  beam on a  $^{nat}\text{Ni}$  target. In this work the beam energy of 160 MeV/nucleon was used, while the value reported in Ref. [33] was measured at 74.5 MeV/nucleon. All values in fb.

This work	B. Blank <i>et al.</i> [33]	EPAX 2.1 [34]	EPAX 3 [28]
$150 \pm 50$	$50 \pm 20$	60	20

## 2. Half-life and branching ratios

Nine events of  $^{48}\text{Ni}$  were registered in the OTPC acquisition system. Two of them did not stop in the active volume of the chamber, so no decay information could be inferred from them. For six events we did observe the decay accompanied by emission of protons. In two of them the stopped ion decayed by emission of a high energy particle, which escaped the active volume of the chamber. This is interpreted as the  $\beta p$  decay of  $^{48}\text{Ni}$ . Four events represented  $2p$  radioactivity of  $^{48}\text{Ni}$ . In two of these the subsequent decay of  $^{46}\text{Fe}$  ( $2p$  daughter of  $^{48}\text{Ni}$ ) by  $\beta$ -delayed proton emission was also recorded, see Fig. 3 in Ref. [17]. Finally, in one event the ion was stopped within the active volume of the chamber but no decay signature was observed during the exposure. Non-observation of such a signature may indicate that either no protons were emitted in the decay or that the decay occurred after the decay gate was closed. Both possibilities are very unlikely, because the  $\beta$  daughter,  $^{48}\text{Co}$  is proton unbound [35] and the  $^{48}\text{Ni}$  half-life is much shorter than the decay gate (see below). It could happen, however, that the decay occurred within the first 100  $\mu\text{s}$  after the implantation when the OTPC is still in the low sensitivity mode. In such case, the signal from the emitted proton would be too weak to be registered. Previously, we have reported two events of this kind [17, 18]. However, after re-analyzing the particle identification as described in section III A, the other event was found to be misidentified.

From the six observed decays of  $^{48}\text{Ni}$  we have determined the half-life using the maximum likelihood method described in Ref. [36]. The result is  $T_{1/2} = 2.1_{-0.6}^{+1.4}$  ms, which is in good agreement with the value reported in Ref. [37].

Based on the observed 4:2 ratio between  $2p$  and  $\beta p$  decay events, the branching ratios were determined to be  $P_{2p} = 0.7(2)$  and  $P_{\beta p} = 0.3(2)$  for the  $2p$  and  $\beta$ -delayed decay channels, respectively. Combined with the measured half-life this yields the partial half-lives of  $T_{1/2}^{2p} = 3.0_{-1.2}^{+2.2}$  ms and  $T_{1/2}^{\beta} = 7.0_{-5.1}^{+6.6}$  ms for  $2p$  and  $\beta$  decay channels, respectively. We note that different branching ratios were determined for  $^{48}\text{Ni}$  in Ref. [37]. Out of the four decay events attributed to  $^{48}\text{Ni}$ , only one was consistent with the  $2p$  emission.

TABLE III. Results of the reconstruction of the four  $2p$  decay events of  $^{48}\text{Ni}$ .  $E_1$  and  $E_2$  are kinetic energies of both protons,  $\theta_{pp}$  is the angle between their momenta,  $E_{rec}$  is the daughter recoil energy, and the  $Q_{2p}$  is the  $2p$  decay energy.

$E_1$ [keV]	$E_2$ [keV]	$\theta_{pp}$ [deg]	$E_{rec}$ [keV]	$Q_{2p}$ [keV]
600(70)	645(110)	66(14)	37(6)	1280 (130)
590(90)	635(90)	36(7)	46(4)	1271 (130)
580(60)	665(50)	51(8)	42(4)	1287 (80)
645(130)	680(80)	33(17)	51(7)	1373 (160)

TABLE IV. Comparison of the determined  $Q_{2p}$  value of  $^{48}\text{Ni}$  with theoretical predictions. All values in MeV.

This work	Brown [38]	Ormand [39]	Cole [40]
1.29(4)	1.36(13)	1.29(33)	1.35(6)

## 3. Two-proton radioactivity

Using the procedure described in Sec. IIIB the four events of  $2p$  radioactivity of  $^{48}\text{Ni}$  were reconstructed. An example of the reconstruction of one event is shown in Fig.11. The results for all four events are presented in Table III. We note that these results differ somewhat from those published previously in Ref. [18] where the simplified reconstruction procedure was used. The weighted average of the  $2p$  decay energy is  $Q_{2p} = 1.29(4)$  MeV. This value agrees very well with theoretical predictions as shown in Table IV.

The measured kinematical data of  $2p$  decays can be transformed to the Jacobi coordinate system which is conventionally used in theoretical description of three-body processes [1, 3]. We consider an initial nucleus at rest which decays by emitting two protons with momenta  $\mathbf{k}_1$  and  $\mathbf{k}_2$  with the decay energy of  $Q_{2p}$ . In the so called T Jacobi coordinate system we define two Jacobi momenta of two-body subsystems:

$$\mathbf{k}_x = \frac{\mathbf{k}_1 - \mathbf{k}_2}{2}, \quad \mathbf{k}_y = \mathbf{k}_1 + \mathbf{k}_2. \quad (5)$$

Then the complete correlation picture is determined by two parameters, the energy fraction  $\varepsilon$  and the angle  $\theta_k$  between the Jacobi momenta  $\mathbf{k}_x$  and  $\mathbf{k}_y$ :

$$\varepsilon = \frac{E_x}{Q_{2p}} = \frac{(k_x^2/m_p)}{Q_{2p}}, \quad \cos(\theta_k) = \frac{(\mathbf{k}_x \cdot \mathbf{k}_y)}{(k_x k_y)}, \quad (6)$$

where  $m_p$  is the proton mass and  $E_x$  is the energy of protons with respect to the center of mass of both protons.

Using the data from Tab. III we arrive at the Jacobi coordinates shown in Fig. 12 together with the correlation picture predicted for the  $2p$  decay of  $^{45}\text{Fe}$  by the three-body model [41]. Although the prediction of the model for the case of  $^{48}\text{Ni}$  is missing, it is expected that the distribution will be qualitatively similar to the case of

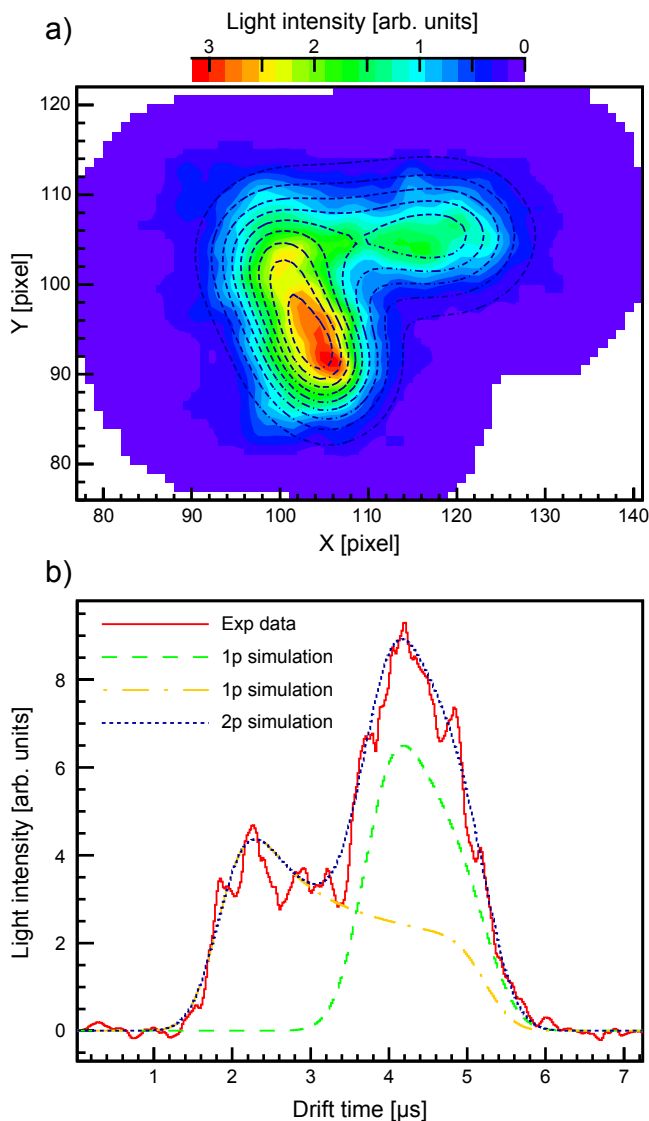


FIG. 11. (Color on-line) An example of reconstruction of a  $2p$  decay event of  $^{48}\text{Ni}$ . a) On the CCD image represented by a color map the best simulation is shown by contour lines. b) The experimental PMT waveform (red histogram) is shown together with lines representing best fitted traces of individual protons and their sum. Both proton tracks originate at about  $5.5 \mu\text{s}$ . The track marked by the yellow line represents the proton emitted towards the anode, hence its Bragg peak appears earlier.

$^{45}\text{Fe}$ . It has a characteristic feature of two bumps, both centered at  $\cos(\theta_k) = 0$  with the smaller one at large values of  $\varepsilon$ . The configuration of both valence protons is assumed to be a mixture of  $f^2$  and  $p^2$  contributions. The relative intensity of this smaller bump reflects the contribution of the  $p^2$  component [42]. Obviously more statistics are needed to establish the experimental distribution for  $^{48}\text{Ni}$ . Presently we can only observe that the four measured points are consistent with the distribution having a maximum at low value of  $\varepsilon$  which corresponds to

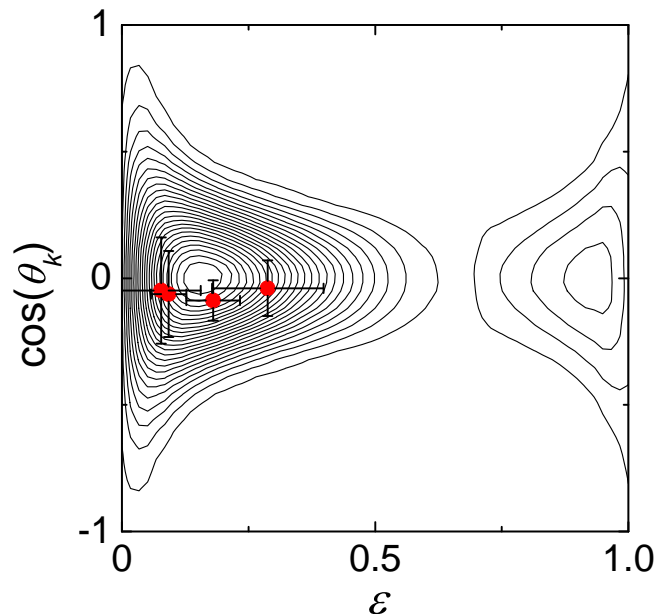


FIG. 12. (Color online) Two-proton momentum correlations from the decay of  $^{48}\text{Ni}$  in the T Jacobi coordinate system, as defined by Eqs. 5,6. It was assumed that the first proton is the one with the lower energy. The opposite assumption would yield the pattern symmetric with respect to the  $\cos(\theta_k) = 0$  line. The experimental points are superimposed on the contour map of the distribution calculated by the three-body model for the  $2p$  decay of  $^{45}\text{Fe}$  [41] (adapted with permission from Ref. [1].)

the low relative energy between protons. This is expected if the initial wave function is dominated by protons in the  $f^2$  configuration [1].

## V. CONCLUSIONS

Using the OTPC detector we have performed proton spectroscopy on nuclei in the vicinity of the presumably doubly-magic  $^{48}\text{Ni}$  which is presently the most neutron-deficient corner of the nuclide chart accessed experimentally ( $T_z = -4$ ). The ions of interest were produced by in-flight fragmentation of a  $^{58}\text{Ni}$  beam at 160 MeV/nucleon on a natural nickel target and selected from the unwanted reaction products by the A1900 fragment separator. The ions of  $^{48}\text{Ni}$  were detected with an average rate of one ion per day with a production cross section of 150(50) fb. Such an efficiency and selectivity of the in-flight technique makes it the method of choice when short-lived very exotic nuclei have to be addressed.

Out of six recorded decays of  $^{48}\text{Ni}$  four decayed by  $2p$  radioactivity. The partial  $2p$  decay half-life was determined to be  $T_{1/2}^{2p} = 3.0_{-1.2}^{+2.2}$  ms. The reconstruction of the proton tracks yielded the total  $2p$  decay energy of  $Q_{2p} = 1.29(4)$  MeV, in good agreement with theoretical

predictions. The momentum correlations between protons in these four events are consistent with the three-body model of  $2p$  radioactivity assuming the dominant  $f^2$  configuration of the protons. A meaningful comparison of the proton correlations with the models of  $2p$  emission requires much larger statistics. This very interesting but ambitious task has to wait for the next generation of radioactive beam facilities.

In addition to  $^{48}\text{Ni}$ , decays of  $^{46}\text{Fe}$  and  $^{44}\text{Cr}$  by  $\beta$ -delayed proton emission were also investigated. Although the experimental conditions were not optimal for this kind of studies, we showed that the OTPC detector can be successfully used to measure proton spectra, especially at low energy. The careful reconstruction of tracks left by delayed protons from  $^{44}\text{Cr}$  yielded the spectrum which shows the same structure as measured previously by an array of silicon detectors [20] but is much cleaner, having no contribution from the  $\beta$  background. The lack of such background allowed to identify a new proton line at 740 keV emitted with probability 0.6% .

Another advantage of the OTPC detector is the accuracy of the branching ratio determination. The direct counting of the incoming, identified ions and of the number of events of a specific decay channel leads to the prob-

ability value which accuracy is essentially limited only by statistics. The possibility to identify unambiguously the decay channel of one event leads to the extreme sensitivity of the OTPC. This was nicely demonstrated by the first observation of the  $\beta$ -delayed two-proton emission from  $^{46}\text{Fe}$  based on one event, even though both protons escaped from the active volume of the detector.

## ACKNOWLEDGMENTS

We gratefully acknowledge the support of the whole NSCL staff during the experiment and, in particular, the efforts of the Operations Group to provide us with the stable, high-intensity beam. This work was supported by the U.S. National Science Foundation under grant number PHY-06-06007, by the U.S. Department of Energy under Contracts DE-AC05-00OR22725 and DE-FG02-96ER40983, by the ORNL LDRD Wigner Fellowship WG11- 035 (KM), by the National Nuclear Security Administration under the Stewardship Science Academic Alliances program through DOE Cooperative Agreement No. DE-FG52-08NA28552, and by the Polish National Science Center under contract no. DEC-2011/01/B/ST2/01943.

- 
- [1] M. Pfützner, M. Karny, L. V. Grigorenko, and K. Riisager, *Rev. Mod. Phys.* **84**, 567 (2012).
- [2] M. J. G. Borge, *Physica Scripta* **T152**, 014013 (2013).
- [3] M. Pfützner, *Physica Scripta* **T152**, 014014 (2013).
- [4] B. Blank and M. Borge, *Progress in Particle and Nuclear Physics* **60**, 403 (2008).
- [5] M. Pfützner, E. Badura, C. Bingham, B. Blank, M. Chartier, H. Geissel, J. Giovinazzo, L. Grigorenko, R. Grzywacz, M. Hellström, Z. Janas, J. Kurcewicz, A. Lalleman, C. Mazzocchi, I. Mukha, G. Mnzenberg, C. Plettner, E. Roeckl, K. Rykaczewski, K. Schmidt, R. Simon, M. Stanoiu, and J.-C. Thomas, *The European Physical Journal A - Hadrons and Nuclei* **14**, 279 (2002).
- [6] J. Giovinazzo, B. Blank, M. Chartier, S. Czajkowski, A. Fleury, M. J. Lopez Jimenez, M. S. Pravikoff, J.-C. Thomas, F. de Oliveira Santos, M. Lewitowicz, V. Maslov, M. Stanoiu, R. Grzywacz, M. Pfützner, C. Borcea, and B. A. Brown, *Phys. Rev. Lett.* **89**, 102501 (2002).
- [7] E. Olsen, M. Pfützner, N. Birge, M. Brown, W. Nazarewicz, and A. Perhac, *Phys. Rev. Lett.* **110**, 222501 (2013); **111**, 139903 (2013).
- [8] B. Blank, A. Bey, G. Canchel, C. Dossat, A. Fleury, J. Giovinazzo, I. Matea, N. Adimi, F. De Oliveira, I. Stefan, G. Georgiev, S. Grévy, J. C. Thomas, C. Borcea, D. Cortina, M. Caamano, M. Stanoiu, F. Aksouh, B. A. Brown, F. C. Barker, and W. A. Richter, *Phys. Rev. Lett.* **94**, 232501 (2005).
- [9] B. Blank, L. Audirac, G. Canchel, F. Delalee, C. Demonchy, J. Giovinazzo, L. Hay, P. Hellmuth, J. Huikari, S. Leblanc, S. List, C. Marchand, I. Matea, J.-L. Pedroza, J. Pibernat, A. Rebi, L. Serani, F. de Oliveira Santos, S. Grvy, L. Perrot, C. Stodel, J. Thomas, C. Borcea, C. Dossat, and R. de Oliveira, *Nuclear Instruments and Methods in Physics Research Section B: Beam Interactions with Materials and Atoms* **266**, 4606 (2008).
- [10] J. Giovinazzo, B. Blank, C. Borcea, G. Canchel, J.-C. Dalouzy, C. E. Demonchy, F. de Oliveira Santos, C. Dossat, S. Grévy, L. Hay, J. Huikari, S. Leblanc, I. Matea, J.-L. Pedroza, L. Perrot, J. Pibernat, L. Serani, C. Stodel, and J.-C. Thomas, *Phys. Rev. Lett.* **99**, 102501 (2007).
- [11] P. Ascher, L. Audirac, N. Adimi, B. Blank, C. Borcea, B. A. Brown, I. Companis, F. Delalee, C. E. Demonchy, F. de Oliveira Santos, J. Giovinazzo, S. Grévy, L. V. Grigorenko, T. Kurtukian-Nieto, S. Leblanc, J.-L. Pedroza, L. Perrot, J. Pibernat, L. Serani, P. C. Srivastava, and J.-C. Thomas, *Phys. Rev. Lett.* **107**, 102502 (2011).
- [12] K. Miernik, W. Dominik, H. Czyrkowski, R. Dąbrowski, A. Fomitchev, M. Golovkov, Z. Janas, W. Kusmierz, M. Pfützner, A. Rodin, S. Stepantsov, R. Slepniev, G. Ter-Akopian, and R. Wolski, *Nuclear Instruments and Methods in Physics Research Section A: Accelerators, Spectrometers, Detectors and Associated Equipment* **581**, 194 (2007).
- [13] K. Miernik, W. Dominik, Z. Janas, M. Pfützner, L. Grigorenko, C. R. Bingham, H. Czyrkowski, M. Ćwiok, I. G. Darby, R. Dąbrowski, T. Ginter, R. Grzywacz, M. Karny, A. Korgul, W. Kuśmierz, S. N. Liddick, M. Rajabali, K. Rykaczewski, and A. Stolz, *Phys. Rev. Lett.* **99**, 192501 (2007).
- [14] K. Miernik, W. Dominik, Z. Janas, M. Pfützner, L. Grigorenko, C. Bingham, H. Czyrkowski, M. Ćwiok, I. Darby, R. Dąbrowski, T. Ginter, R. Grzywacz, M. Karny,

- A. Korgul, W. Kusmierz, S. Liddick, M. Rajabali, K. Rykaczewski, and A. Stolz, *The European Physical Journal A* **42**, 431 (2009).
- [15] K. Miernik, W. Dominik, Z. Janas, M. Pfützner, C. R. Bingham, H. Czyrkowski, M. Ćwiok, I. G. Darby, R. Dąbrowski, T. Ginter, R. Grzywacz, M. Karny, A. Korgul, W. Kuśmierz, S. N. Liddick, M. Rajabali, K. Rykaczewski, and A. Stolz, *Phys. Rev. C* **76**, 041304 (2007).
- [16] M. Pomorski, K. Miernik, W. Dominik, Z. Janas, M. Pfützner, C. R. Bingham, H. Czyrkowski, M. Ćwiok, I. G. Darby, R. Dąbrowski, T. Ginter, R. Grzywacz, M. Karny, A. Korgul, W. Kuśmierz, S. N. Liddick, M. Rajabali, K. Rykaczewski, and A. Stolz, *Phys. Rev. C* **83**, 014306 (2011).
- [17] M. Pomorski, M. Pfützner, W. Dominik, R. Grzywacz, T. Baumann, J. S. Berryman, H. Czyrkowski, R. Dąbrowski, T. Ginter, J. Johnson, G. Kamiński, A. Kuźniak, N. Larson, S. N. Liddick, M. Madurga, C. Mazzocchi, S. Mianowski, K. Miernik, D. Miller, S. Paulauskas, J. Pereira, K. P. Rykaczewski, A. Stolz, and S. Suchyta, *Phys. Rev. C* **83**, 061303 (2011).
- [18] M. Pomorski, M. Pfützner, W. Dominik, R. Grzywacz, T. Baumann, J. S. Berryman, H. Czyrkowski, R. Dąbrowski, T. Ginter, J. Johnson, G. Kamiński, A. Kuźniak, N. Larson, S. N. Liddick, M. Madurga, C. Mazzocchi, S. Mianowski, K. Miernik, D. Miller, S. Paulauskas, J. Pereira, K. P. Rykaczewski, A. Stolz, and S. Suchyta, *Acta Phys. Pol.* **B43**, 267 (2012).
- [19] M. Pomorski, M. Pfützner, W. Dominik, R. Grzywacz, T. Baumann, J. S. Berryman, C. R. Bingham, H. Czyrkowski, M. Ćwiok, I. G. Darby, R. Dąbrowski, T. Ginter, L. Grigorenko, Z. Janas, J. Johnson, G. Kamiński, M. Karny, A. Korgul, W. Kuśmierz, A. Kuźniak, N. Larson, S. N. Liddick, M. Madurga, C. Mazzocchi, S. Mianowski, K. Miernik, D. Miller, S. Paulauskas, J. Pereira, M. Rajabali, K. P. Rykaczewski, A. Stolz, and S. Suchyta, in *American Institute of Physics Conference Series*, American Institute of Physics Conference Series, Vol. 1409, edited by B. Blank (2011) pp. 83–86.
- [20] C. Dossat, N. Adimi, F. Aksouh, F. Becker, A. Bey, B. Blank, C. Borcea, R. Borcea, A. Boston, M. Caamano, G. Cachel, M. Chartier, D. Cortina, S. Czajkowski, G. de France, F. de Oliveira Santos, A. Fleury, G. Georgiev, J. Giovinazzo, S. Grvy, R. Grzywacz, M. Hellstrm, M. Honma, Z. Janas, D. Karamanis, J. Kurcewicz, M. Lewitowicz, M. L. Jimnez, C. Mazzocchi, I. Matea, V. Maslov, P. Mayet, C. Moore, M. Pfützner, M. Pravikoff, M. Stanoiu, I. Stefan, and J. Thomas, *Nuclear Physics A* **792**, 18 (2007).
- [21] D. Morrissey, B. Sherrill, M. Steiner, A. Stolz, and I. Wiedenhoever, *Nuclear Instruments and Methods in Physics Research Section B: Beam Interactions with Materials and Atoms* **204**, 90 (2003).
- [22] O. Tarasov and D. Bazin, *Nuclear Instruments and Methods in Physics Research Section B: Beam Interactions with Materials and Atoms* **266**, 4657 (2008).
- [23] F. Sauli, *Nuclear Instruments and Methods in Physics Research Section A: Accelerators, Spectrometers, Detectors and Associated Equipment* **386**, 531 (1997).
- [24] M. Lourakis, “levmar: Levenberg-marquardt nonlinear least squares algorithms in C/C++,” [web page] <http://www.ics.forth.gr/~lourakis/levmar/> (Jul. 2004), [Accessed on 31 Jan. 2005].
- [25] J. Ziegler, “The stopping and range of ions in matter (srim),” [web page] <http://www.srim.org>.
- [26] B. Blank, S. Andriamonje, R. Del Moral, J. P. Dufour, A. Fleury, T. Josso, M. S. Pravikoff, S. Czajkowski, Z. Janas, A. Piechaczek, E. Roeckl, K.-H. Schmidt, K. Sümmerer, W. Trinder, M. Weber, T. Brohm, A. Grewe, E. Hanelt, A. Heinz, A. Junghans, C. Röhl, S. Steinhäuser, B. Voss, and M. Pfützner, *Phys. Rev. C* **50**, 2398 (1994).
- [27] D. J. Morrissey, *Phys. Rev. C* **39**, 460 (1989).
- [28] K. Sümmerer, *Phys. Rev. C* **86**, 014601 (2012).
- [29] R. Barlow, arXiv:physics/0406120.
- [30] M. Wang, G. Audi, A. Wapstra, F. Kondev, M. MacCormick, X. Xu, and B. Pfeiffer, *Chinese Physics C* **36**, 1603 (2012).
- [31] O. Tarasov, D. Bazin, T. Baumann, A. Gade, T. Ginter, M. Hausmann, D. Morrissey, J. Pereira, M. Portillo, B. Sherrill, A. Stolz, and M. Thoennessen, *Nuclear Instruments and Methods in Physics Research Section A: Accelerators, Spectrometers, Detectors and Associated Equipment* **620**, 578 (2010).
- [32] O. Tarasov, *Nuclear Physics A* **734**, 536 (2004), `ixocs:full-name;Proceedings of the Eighth International Conference On Nucleus-Nucleus Collisions;ixocs:full-name;.`
- [33] B. Blank, M. Chartier, S. Czajkowski, J. Giovinazzo, M. S. Pravikoff, J.-C. Thomas, G. de France, F. de Oliveira Santos, M. Lewitowicz, C. Borcea, R. Grzywacz, Z. Janas, and M. Pfützner, *Phys. Rev. Lett.* **84**, 1116 (2000).
- [34] K. Sümmerer and B. Blank, *Nuclear Physics A* **701**, 161 (2002).
- [35] T. Burrows, *Nuclear Data Sheets* **107**, 1747 (2006).
- [36] K.-H. Schmidt, C.-C. Sahn, K. Pielenz, and H.-G. Clerc, *Zeitschrift für Physik A Atoms and Nuclei* **316**, 19 (1984).
- [37] C. Dossat, A. Bey, B. Blank, G. Cachel, A. Fleury, J. Giovinazzo, I. Matea, F. d. O. Santos, G. Georgiev, S. Grévy, I. Stefan, J. C. Thomas, N. Adimi, C. Borcea, D. C. Gil, M. Caamano, M. Stanoiu, F. Aksouh, B. A. Brown, and L. V. Grigorenko, *Phys. Rev. C* **72**, 054315 (2005).
- [38] B. A. Brown, *Phys. Rev. C* **43**, R1513 (1991).
- [39] W. E. Ormand, *Phys. Rev. C* **55**, 2407 (1997).
- [40] B. J. Cole, *Phys. Rev. C* **54**, 1240 (1996).
- [41] L. V. Grigorenko, I. A. Egorova, M. V. Zhukov, R. J. Charity, and K. Miernik, *Phys. Rev. C* **82**, 014615 (2010).
- [42] L. V. Grigorenko and M. V. Zhukov, *Phys. Rev. C* **68**, 054005 (2003).